Polymorphism of VO2 thin film: M1, T, and M2 single phase synthesis using pulsed laser deposition

Yannick Bleu, Florent Bourquard, Konstantinos Misdanitis, Anthony Poulet, Anne-Sophie Loir, Florence Garrelie, Christophe Donnet

Version of Record: https://www.sciencedirect.com/science/article/pii/S2352492823002544
Manuscript_bee40326c4b0a82770b0c7f8fa0e3ce7

Polymorphism of VO_2 thin film: M1, T, and M2 single phase synthesis using pulsed laser deposition

Yannick Bleu, Florent Bourquard, Konstantinos Misdanitis, Anthony Poulet, Anne-Sophie Loir, Florence Garrelie, Christophe Donnet

Université de Lyon, Université Jean Monnet-Saint-Étienne, CNRS, Institut d'Optique Graduate School, Laboratoire Hubert Curien, UMR 5516, F-42023 Saint-Étienne, France

Abstract

Vanadium dioxide (VO_2) can undergo a reversible insulator-to-metal transition (IMT) along with a structural phase transition from monoclinic M1 to rutile tetragonal R at about 68ºC, thereby making a range of optic and electronic applications possible. The structural phase transition from monoclinic M1 to rutile tetragonal R can occur via two other intermediate metastable phases of triclinic T and monoclinic M2. Due to their narrow thermodynamic stability, selective phase deposition of VO_2 thin films is a major challenge. In the present study, apart from synthesizing the VO_2 thin film with M1 phase, we also selectively elaborated the T and M2 phases using pulsed laser deposition (PLD) by simply controlling the repetition rate of the laser. Analysis of the structural, morphological, nanomechanical, thermochromic, and optical properties of each of these polymorphs demonstrated strong dependence of these properties on the VO_2 phases, and hence on the laser repetition rate. The ability to stabilize different polymorphs of VO_2 thin films paves the way for novel structures that are promising for new device functionalities.

Keywords: VO_2 polymorphism, Pulsed laser deposition, laser repetition rate, phase transition, surface morphology, nanomechanical, optical properties.

1. Introduction

Vanadium dioxide (VO_2) exhibits various polymorphic forms. The most frequently studied phase is the monoclinic VO_2 (M1), which, in its pure form undergoes an IMT into the rutile VO_2(R) phase at 68°C. Other phases are triclinic VO_2 (T), monoclinic VO_2 (M2), tetragonal VO_2 (A) and monoclinic VO_2 (B) phases**[1–5]**. In terms of structure, in the M1 phase, all the vanadium ions are dimerized and tilted in equivalent chains with a space group of $P2_1/c$. The M2 phase, with a space group of C2/m, contains two distinct types of vanadium chains. The first type of chain type is formed of vanadium ions that dimerize but do not tilt, and the second type consists of vanadium ions that twist but do not pair. The T phase comprises two types of non-equivalent vanadium chains in which the vanadium ions are dimerized and twisted to different degrees with a space group of P1**[6]**. Phase T is commonly considered to be an intermediate phase between phases M2 and M1, in which the chains become equivalent in M1. Among these three phases, the M1 phase is well known and there is rich literature about the M2 phase. Whereas the other T phase has received little attention despite its ability to lead, to different phase transition behaviors and properties due to its metastable structures**[7,8]**. However, it has been reported that the stabilization of T and M2 phases can be achieved by oxygen non-stoichiometry**[9,10]**, by incorporating impurities via doping**[5,11–13]**, and by external strain**[14,15]**.

Since both doping and strain cause remarkable structural distortion of VO_2 structures and modify their intrinsic properties and applications, an effective strategy is required to engineer VO_2 thin film with stabilized multi-phases. Different synthesis techniques have been developed and used to stabilize these VO_2 thin film polymorphs. It has been reported that using the pulsed laser deposition (PLD) technique, VO_2 thin films with M1, M2, T, and R phases, can be stabilized by using a buffer layer**[16,17]** as well as by incorporating dopants**[18]**. Recently, R. McGee et al.**[19]** reported stabilizing the T phase by optimizing the deposition process, including laser energy, substrate temperature, target-to-substrate distance, and oxygen pressure. Srivastava et al.**[20]** grown selectively the single phase of VO_2 (A, B, and M) by tuning the laser repetition rate and the oxygen background pressure. Furthermore, Jian et al.**[21]** reported the effect of the laser repetition rate on the VO_2 microstructure. Despite these studies, controlling the stabilization of VO_2 phases remains a major challenge. Finding simple ways to synthesize specific VO_2 polymorphs with well-defined properties will pave the way for manufacturing new devices.

In this study, we stabilized monoclinic VO_2 (M1), triclinic VO_2 (T) and monoclinic VO_2 (M2) thin films on fused silica substrates using PLD. This was done simply by varying the repetition rate of the laser at a constant energy density, thereby by changing the rate of arrival of plasma species on the surface of the substrate while keeping the other growth parameters fixed. Here, we report the investigation of the structural, morphological, nanomechanical properties, as well as the thermochromic and optical properties including the transition temperature, the hysteresis width, the absorbance in the visible ranges, and the optical energy gap of each VO_2 phase. Our results point to the powerful modulation capability of the PLD process to selectively stabilize VO_2 thin film phases.

2. Experimental details

Synthesis of VO_2 thin films

Vanadium dioxide (VO_2) thin films were grown using a two-step process: pulsed laser deposition (PLD) of V_2O_5 followed by rapid thermal annealing, as shown in Fig.1.

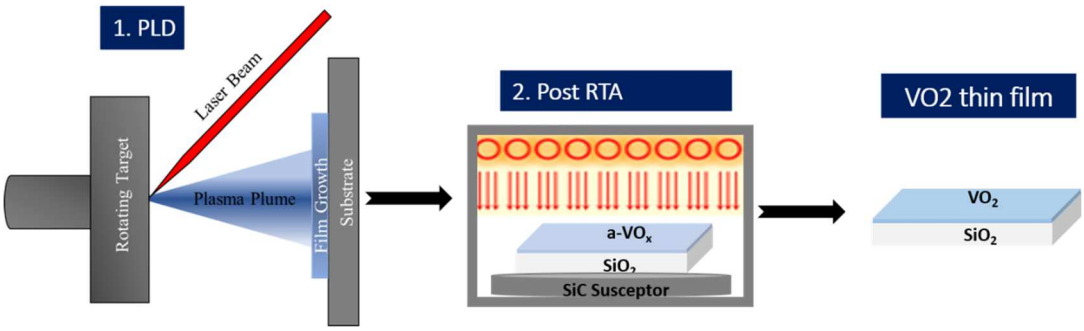

Figure 1: Schematic illustration of the VO_2 films synthesis using pulsed laser deposition and ex-situ rapid thermal annealing on SiO_2. The laser repetition rate was fixed to 10, 20 or 40 Hz. All the other synthesis parameters were also fixed.

The energy source for the PLD experiment was a KrF excimer laser (Lambda-Physik LPX 200) operating at 248 nm and a 20-nanosecond pulse duration. The target material was pure vanadium pentoxide (V2O5) (99.99% from NEYCO, France) and the substrate sample was fused silica (SiO2). To minimize the formation of craters, the target was rotated during laser ablation of material with a target-to-substrate distance of 5 cm and at a 45° angle to the target surface. The laser fluence was kept steady at 8.6 J/cm2 and the thin films were deposited using different repetition rates (10, 20 and 40 Hz) under high vacuum (5.10-6 mbar) in the deposition chamber. For each rate, the deposition time was optimized to obtain a film of similar thickness (20 nm). An ex-situ rapid post thermal annealing process was performed

after PLD deposition at 400 °C with a heating step of 5 °C /s and oxygen 1 mbar pressure with a 50 sccm flow, a dwelling time of 120 s followed by natural cooling.

Characterization

The structural, morphological, nanomechanical and optical properties of the VO_2 thin films were characterized. Raman analysis (Jobin-Yvon ARAMIS) was carried out using a helium neon laser source at an excitation wavelength of 633 nm, with a laser power of 0.1 mW, and a laser beam focused by a 100x objective, consistent with a laser spot diameter of less than 1 mm. Scanning electron microscopy (SEM) (JEOL IT 800 SHL) was used to analyze the morphology. Atomic force microscopy (AFM) (Icon BRUKER) measurements were made to analyze the topography, the roughness of the films and the nanomechanical properties in the quantitative nanomechanical (QNM) mode. Each scan was performed at a rate of 0.5 Hz and a scan size of 512 x 512 points. The AFM-QNM was operated in tapping mode under ambient conditions using a RTESPA 300-30 tip with a spring constant of 60 N/m and a radius of 28 nm after calibration. The tip used has an antimony (n) doped Si cantilever, coated by reflective Al-layer (L = 125 μm; W = 40 μm; d = 3.4 μm; f_0 = 300 kHz). All the images were recorded using the Nanoscope controller V and analyzed with Nanoscope analysis and Gwyddion softwares. UV–Visible spectroscopy in absorbance mode was conducted in the spectral range between 200–900 nm at room temperature. The thermochromic properties of the films were determined by collecting the transmittance in the temperature range of 20-100 °C using a fiber optic spectrometer in visible (400-800 nm) and IR (900-2500 nm) wavelength ranges and equipped with handmade heating units.

3. Results and discussion

1. Structural and morphological analysis

After synthesis, Raman spectroscopic measurements were taken to confirm the three different VO_2 phases. As Raman spectroscopy is sensitive to subtle structural changes, the evidential blue-shift of A_g phonon mode from 610 to 650 cm^{-1} corresponding to V-O bonding is usually used to distinguish the VO_2 phases and to trace their phase transitions. In Raman spectra, this high frequency V-O stretching mode is usually located at < 615 cm^{-1} in the M1 phase, at > 647 cm^{-1} in the M2 phase, and within the 615–646 cm^{-1} range in the T phase**[4,14]**. Our room temperature Raman spectroscopy confirmed stabilization of the M1, T and M2 phases. Fig. 2a

shows the Raman spectra of the three different thin films with the M1, T, and M2 phases identified in comparison with data in the literature **[4,14,22–25]**. In the Raman spectrum of the VO_2 (M1), peaks were observed at 125,196(A_g), 224(A_g), 268(A_g/B_g), 308(A_g), 340(A_g), 385(A_g/B_g), 441(A_g/B_g), 498(A_g/B_g), 622(A_g), and 828 (B_g) cm^{-1} that were all attributed to M1 phase Raman modes**[22]**. In the VO_2 (T) thin film, peaks have been observed at 120, 200(A_g), 226(A_g), 274(A_g/B_g), 303(A_g), 340(A_g), 440(A_g/B_g), 499(A_g/B_g), 639(A_g), and 830(Bg) that were all attributed to T phase Raman modes**[23,24]**. The strongest peak located at 639 cm^{-1} and the low frequency mode at 200 cm^{-1} are characteristic of the T phase in contrast to peaks at 622 cm^{-1} and 198 cm^{-1} in the M1 phase. Lastly, in the VO_2 (M2) thin film, nine distinct peaks were observed at 118, 205(A_g), 225(A_g), 277(A_g/B_g), 300(A_g), 338(A_g), 440(A_g/B_g), 495(A_g/B_g), 646(A_g), and 832(B_g) cm^{-1} that were identical to those of the M2 phase**[23,24]**.

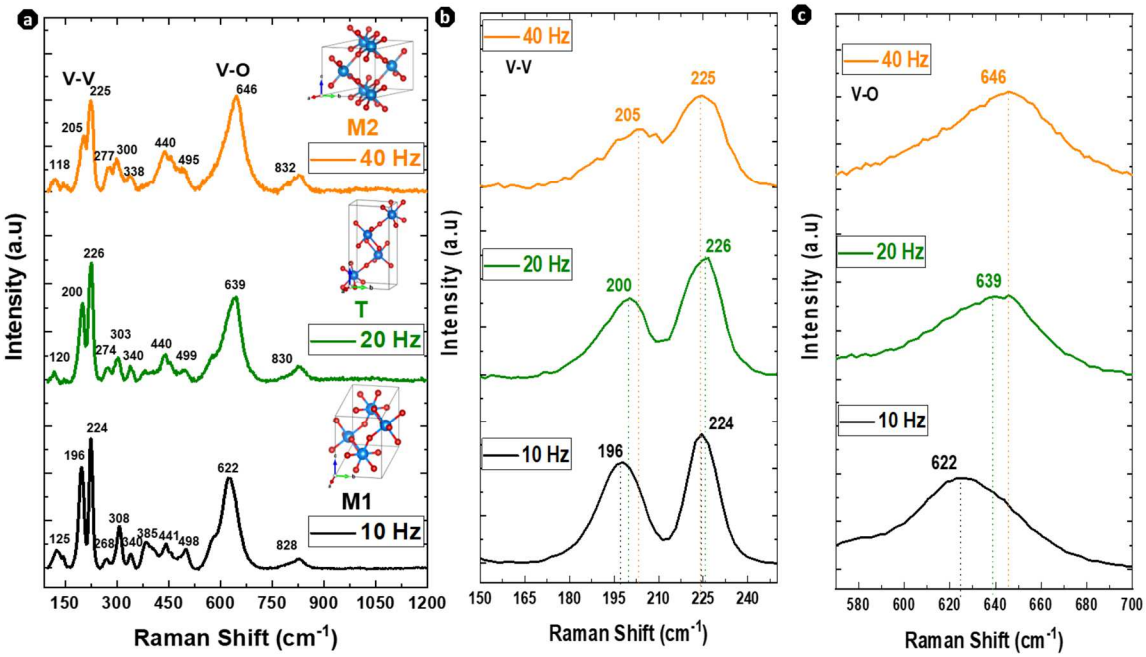

Figure 2. (a) Raman spectra of three VO_2 thin film phases (M1 in black, T in green and M2 in orange) with unit cell representations of the M1, T, and M2 crystal structures. (b) Zoomed view of A_g Raman peaks around 196 and 224 cm^{-1}. (c) Zoomed view of A_g Raman spectra at approximately 622 cm^{-1}.

The lowest peak located around 125 - 118 cm^{-1} is usually found at 141 cm^{-1} and its interpretation is not always clear and still under debate. Previous works**[24–26]** assigned this peak to A_g vibrational mode. However, other studies**[27,28]** reported that this peak can be excited by the external mode as layered modes in V_2O_5. In our experiment, since we used V_2O_5 as a precursor for the thin film deposition, we suggest that this peak is related to the external mode excited by some trace of V_2O_5.

To further investigate the difference between the phases, we enlarged the low frequency V−V vibration modes around 196 and 224 cm^{-1} and the high frequency V-O bond around 622 cm^{-1} in the three samples as shown in Figs. 2b and c. The V–V mode is located around 196 and 224 cm^{-1} for the M1 phase, 200 and 226 cm^{-1} for the T phase, and 205 and 225 cm^{-1} for the M2 phase. This is evidence for a frequency shift of 4 and 9 cm^{-1} from M1 to T and M1 to M2, respectively, considering the A_g mode at 196 cm^{-1}. In addition, the weakening of the intensity associated to this slight shift of the 196 cm^{-1} mode confirmed the phase change. The strongest peak corresponding to the V-O bond stretching vibration occurred at 622 cm^{-1} in the M1 phase. A huge frequency shift from 622 cm^{-1} mode to around 639 and 646 cm^{-1} shows a transition from the M1 phase to the T and M2 phases, respectively. Therefore, our Raman analysis confirmed stabilization of three different phases of VO_2 (M1, T and M2) thin films. According to the literature, C. Marini, et al.**[29]** suggested that the presence of oxygen non-stoichiometry as well as the impurities can stabilize the VO_2 M2 phase. Others studies**[24,30]** observed that Raman spectra of non-stoichiometric VO_2 lead to the shift to higher frequency due to compressive stress. S. Zhang, et al.**[9]** used only Raman analysis to differentiate between M1, T and M2 phases with the shift of the peak positions. And other studies reported that oxygen vacancies can work as electron dopants that stabilize the rutile R phase **[31]**, while the high oxygen content and the presence of V^{5+} ions in the VO_2 structure probably lead to the formation of the M2 phase and T phase**[9,10]**. Therefore, our results being consistent with the previous works, we suggest that the stabilization of T and M2 phases can be explained by the strain/stress introduced via the variation in VO_2 stoichiometry which can be caused by oxygen non-stoichiometry or other impurities.

Indeed, the spatial laser pulse overlap O can play a role during the ablation of the V_2O_5 target. This parameter is defined as the dimensionless number of incident laser pulses per illuminated area obtained from the following relation**[32]**:

$$O = \frac{W.R}{S} \quad (1)$$

where W is the diameter of the spot (in mm), R is the laser pulse repetition rate (in Hz), and S is the scan speed (in mm/s). The spot diameter W is estimated at 1.2 mm, and the scan speed is obtained using the target angular speed during laser ablation (10 rotations in 16 seconds) and the perimeter of the scan path 2πr with r the radius of the scan path (r = 6 mm):

$$S = \left(\frac{10\ \text{trs}}{16\ \text{s}}\right).2.\pi.6\ (\text{mm}) = 23.6\ \text{mm/s} \quad (2)$$

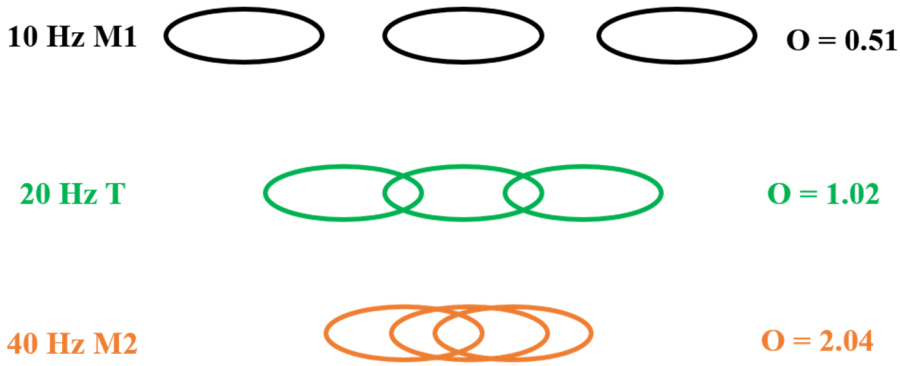

Figure 3: Illustration of the spatial laser pulse overlap O with its different values for the three repetition rates, related to the laser irradiation on the rotating V_2O_5 target.

We observed that when the repetition rate increased, the laser overlap also increased. This means that at the higher repetition rate R = 40 Hz, the interval between two consecutive pulses was shorter, as illustrated in Fig.3, and that the ablated target has less time to cool down between each laser pulse than at lower repetition rates. Therefore, the dependence of the laser pulse overlap on the repetition rate results in the production of different plasma composition during ablation, which probably gives rise to different VO_x phases following pulsed laser deposition, and hence to different VO_2 phases after the post-annealing. Indeed, the few published works**[32–34]** explained the laser repetition rate effect on the growth of thin films by a reduction or an increase in the length of the interval between the deposition of two sequential pulses, just as we did. However, the laser-target interaction mechanism during ablation when the laser repetition rate changes remains to be elucidated.

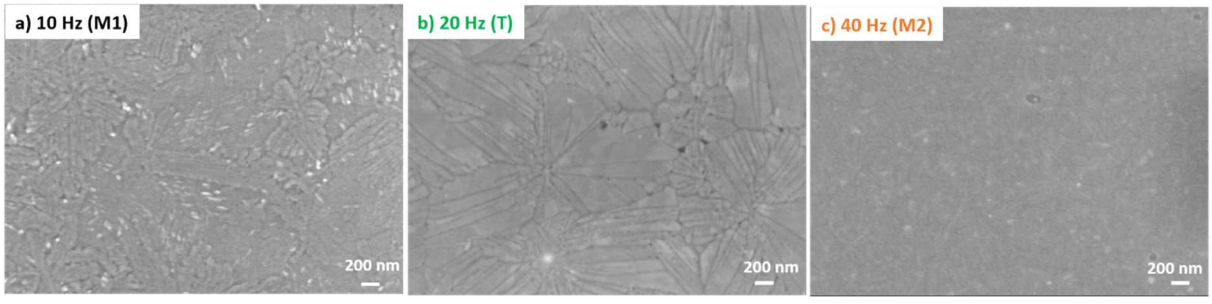

Figure 4. FE-SEM images of the surface of synthesized VO_2 at three different laser pulse repetition rates: (a) 10 Hz, (b) 20 Hz, (c) 40 Hz.

Controlling the morphology and surface roughness of the film is important because these parameters play a crucial role in both the optical and electrical behavior of the film**[35,36]**. Fig. 4 shows the SEM images for the three VO_2 samples. These images show that the surface

of all three samples was completely covered but that the morphologies differ. The sample with the M1 phase has a rougher surface, the sample of T phase VO_2 a flat structure with cracks, whereas the M2 phase has no cracks.

We also measured surface roughness using AFM to understand how the deposition parameters influence the resultant morphology of the thin films. The topographical AFM images of the three VO_2 samples are presented in Fig. 5. The images show that the three samples have completely different topographies similar to that was observed in the SEM images. The sample with the M1 phase had a rough surface, while surfaces of the samples of the T and M2 phases were smoother and their roughness values were similar. Indeed, an increase in the laser repetition rate reduced surface roughness, in agreement with one report **[33]** stating that varying the repetition rate can affect surface roughness, i.e., from the M1 to the M2 phase, the VO_2 becomes smoother. As all the other process parameters were kept constant, this difference in surface morphology can only be due to the change in the laser repetition rate. The increase in the laser repetition rate reduces the length of the interval between the sequent shots, namely, the island ripening time decreases. Therefore, at the highest repetition rate f = 40 Hz, the interval time between two sequent pulses is reduced, whereas when the pulse frequency f = 10 Hz, the interval between two laser pulses is longer, allowing longer for the adatoms on the substrate surface to diffuse. We therefore concluded that the surface morphology of the VO_2 thin film is strongly dependent on the laser repetition rate.

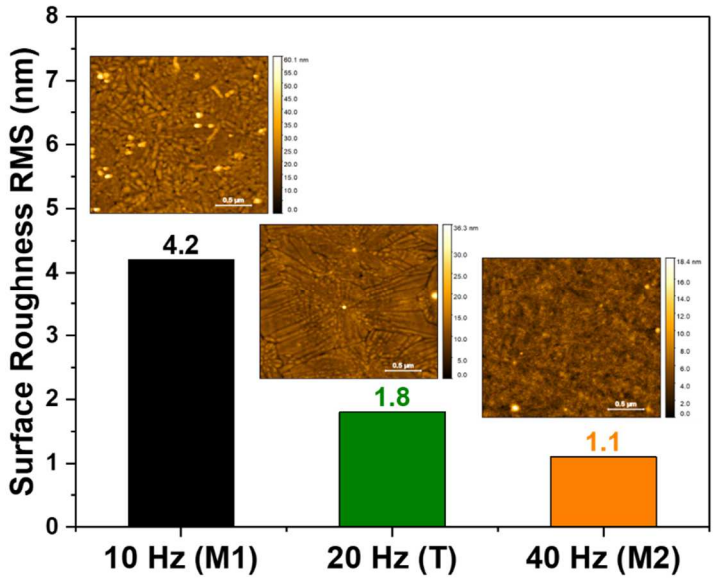

Figure 5. Plot of surface roughness as a function of the different VO_2 phases obtained at different laser repetition rates. The inserts are the corresponding AFM images, the scale bar in the images is 0.5 µm.

2. *Nanomechanical properties: DMT modulus and adhesion force*

QNM studies of the three VO_2 phases were undertaken to understand some of their mechanical behaviors at the nanoscale. The results are presented in the form of DMT maps of Young's modulus (elasticity) and adhesion force in Fig. 6. The color code provides further detailed information about variations in these nanomechanical properties. The distributions of the DMT modulus and adhesion force are shown in their respective histograms also in Fig 6. The DMT modulus is Young's modulus calculated using the Derjaguin–Muller–Toporov (DMT) model of elastic interaction due to taking the adhesion force into consideration **[37]**. It is also called reduced Young's modulus, related to the sample modulus via the following equation (3):

$$E^* = \left[\frac{1-\nu_s^2}{E_s} + \frac{1-\nu_{tip}^2}{E_{tip}}\right]^{-1} \quad (3)$$

where E_s is the sample modulus, E_{tip} the tip modulus, ν_s the sample Poisson ratio, and ν_{tip} the tip Poisson ratio. In our experiment, the calculations of the modulus with the DMT model were imaged in real time during scanning.

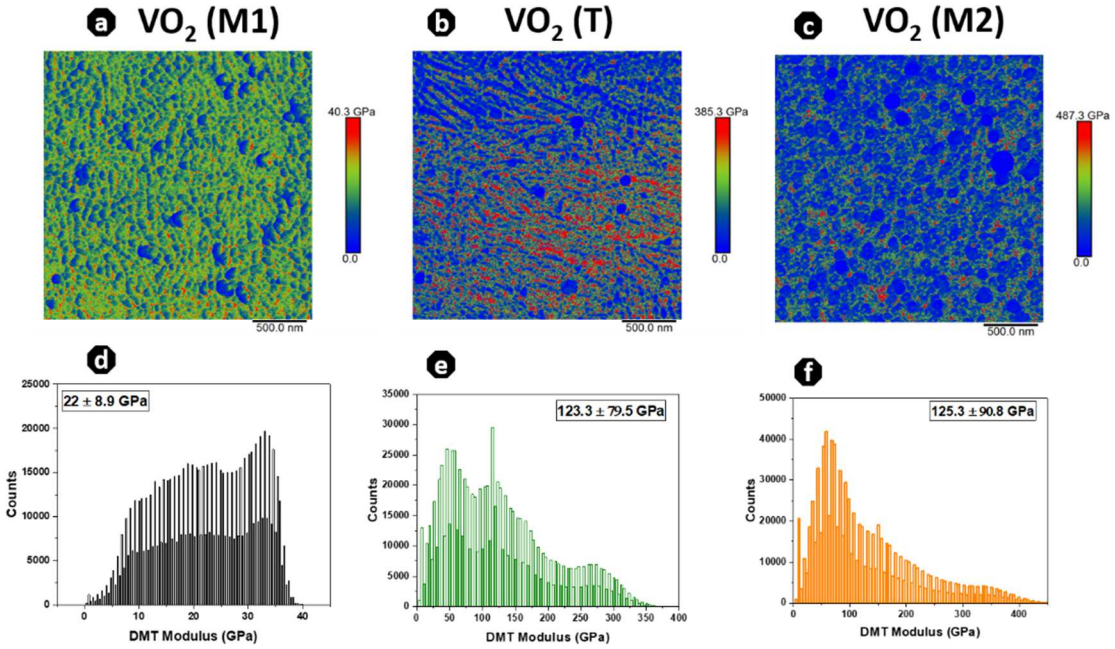

Figure 6. Representative map of the DMT modulus (2.5 x 2.5 µm²) for samples (a)VO_2 (M1), (b), VO_2 (T), (c) VO_2 (M2), and (d–f) the corresponding histogram of the distribution of the DMT modulus with the mean values.

Fig. 6 shows the resulting DMT modulus maps of each VO_2 phase. It can be seen that the VO_2 (M1) thin film surface over the entire tested area is characterized by a non-uniform value of the Young's modulus, highlighted by the high dispersion of the values on the histogram of the DMT modulus (Fig. 5a) over the range 13 to 31 GPa, with the mean value around 22 GPa. The DMT modulus of the VO_2 (T and M2) phases present even greater dispersion values, i.e. from 44 to 202, and from 35 to 215 GPa, respectively, compared to the VO_2 (M1) as shown in Fig. 6b and c and in their corresponding histograms (Fig. 6e and f). Comparing the average DMT modulus values, these two phases present a much higher DMT modulus than the other M1 phase. In the literature, the Young modulus of vanadium oxide films has been reported to be in a wide range, i.e. 5.6 GPa to 140 GPa**[38–40]**. As we were unable to find any other studies in the literature reporting the nanomechanical measurement of VO_2 thin film using AFM-QNM, we compared our results with Young's modulus obtained using other methods. The DMT modulus values of three VO_2 phases are thus in line with what can be found in the literature, even though the standard deviation is also large due to the inconsistency of our samples. The difference in the DMT modulus between the M1 and T-M2 phases could be due to differences in their morphologies, grain size and surface roughness. Indeed, it has been reported that a less porous thin film with small grain size and lower roughness can produce a high Young modulus**[41]**. We believe that this may be the case in our study since the VO_2 (M1) phase has a larger grain size and is rougher than the two other phases.

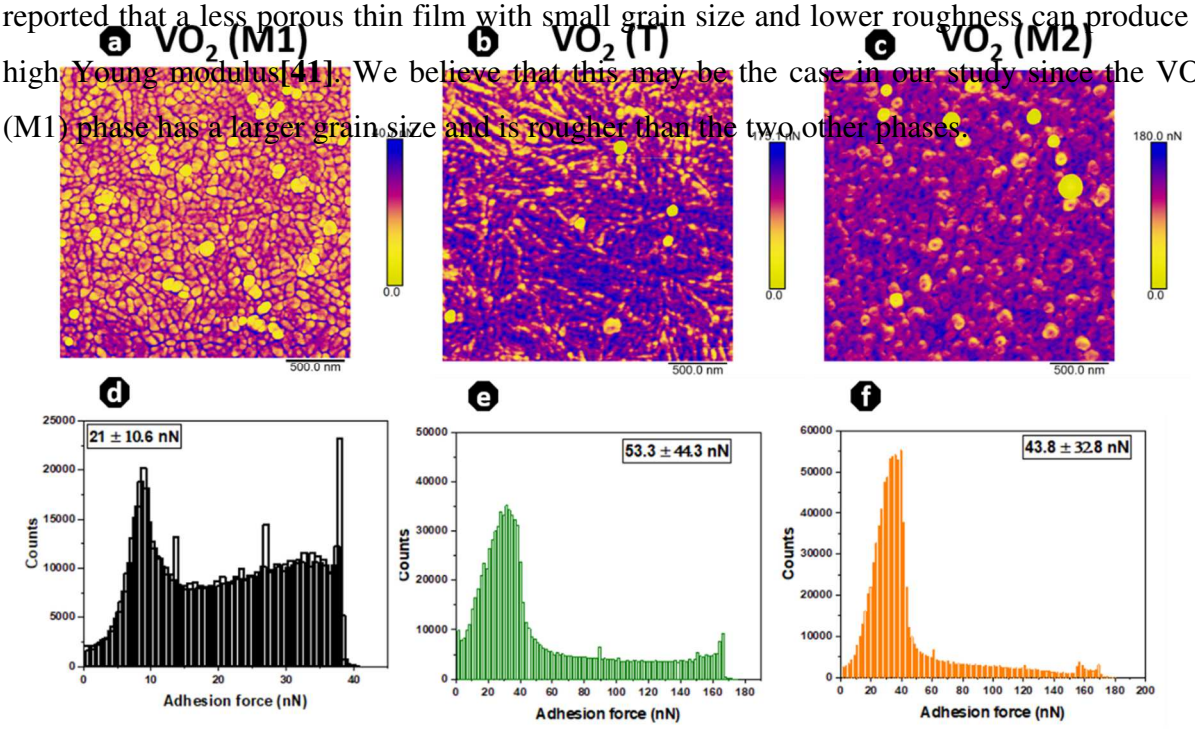

Figure 7. Representative map of the adhesion forces (2.5 x 2.5 µm²) for samples (a)VO_2 (M1), (b), VO_2 (T), (c) VO_2 (M2), and (d–f) the corresponding histogram of the distribution of the adhesion forces with the mean values.

The second nanomechanical property acquired in the mapping was the adhesion force, which is an important parameter for mechanical systems. Like the DMT modulus value in the M1 phase sample, adhesion forces were not homogeneous over the whole area scanned. The histogram of adhesion distribution showed scatter of the obtained values ranging from 10 to 32 nN, with an average value of 22 nN. With the VO_2 (T and M2) phases, there was an increase in adhesive forces with mean values of 53.3 and 43.8 nN for the sample T and M2 phases, respectively, as shown in Fig.7. The corresponding histograms (Fig. 7d–f) show an increase in the dispersion of the measured adhesion forces that reached values ranging from 9 to 97 nN, and from 12 to 76 nN, respectively. Again, like in the DMT modulus results, adhesion force of the M1 phase was lower than that of the two other phases (T and M2) whose adhesion force values were close. It has been reported that the large surface energy and higher adhesion of ZnO films was due to weaker crystallization and smaller grain sizes**[42]**. Therefore, like for DMT modulus, we suggest that the difference in the adhesion force between M1 and T-M2 phases is linked to their microstructure. Since, to the best of our knowledge, there is no literature on the adhesion forces of vanadium oxides, we recommend further AFM-QNM investigations to corroborate and discuss the relationships between the nature of the VO_2 phases and their nano-mechanical properties.

3. Thermochromic and optical properties

The transition temperature (T_t) of IMT is one of the most basic characteristics of the thermochromic properties of VO_2. To identify this parameter in the three VO_2 thin films during the phase transition, we measured the temperature-dependent transmittance curves (transmittance vs temperature) from 20-100 °C, as illustrated in Fig. 8a, and the value of T_t in all samples was obtained by Gaussian fitting (Fig. 7b) extracted from the dTr/dT curves shown in Fig. 8a.

The transition temperature of a sample of the VO_2 (M1) phase was 56 °C with a hysteresis width value of 14 °C. This reduced T_t in the M1 phase is probably due to the oxygen deficiency in the thin film**[5]**. Indeed, it has been reported that the stoichiometry of VO_2

significantly affects the temperature transition and phases. Oxygen vacancies can function as electron dopants which stabilize the metallic R phase at reduced temperatures**[5,31]**, while the high oxygen content and the presence of V^{5+} ions in the VO_2 lattice lead to the formation of the M2 and T phases**[9,10]**. With the VO_2 (T) phase, T_t significantly increased to 71 °C with a reduced hysteresis width ΔT (9 °C) and in the M2 phase, T_t reached the highest point of 81 °C, with a ΔT of 6 °C. Basu et al.**[23]** reported a transition temperature of 348 K (75 °C) for the T phase and 355K (82 °C) for the M2 phase, which are similar to that obtained in the present study. Furthermore, it has been reported that the T_t of VO_2 can be shifted to higher temperatures either by doping VO_2 with specific elements such as Al, Cr or Ge**[43,44]**, or by strain**[14,23]**. Since the samples used in our experiment were not doped, we suggest that the increase of IMT value associated with the stabilized VO_2 (T and M2) phases, may be linked to the strain caused by excess oxygen.

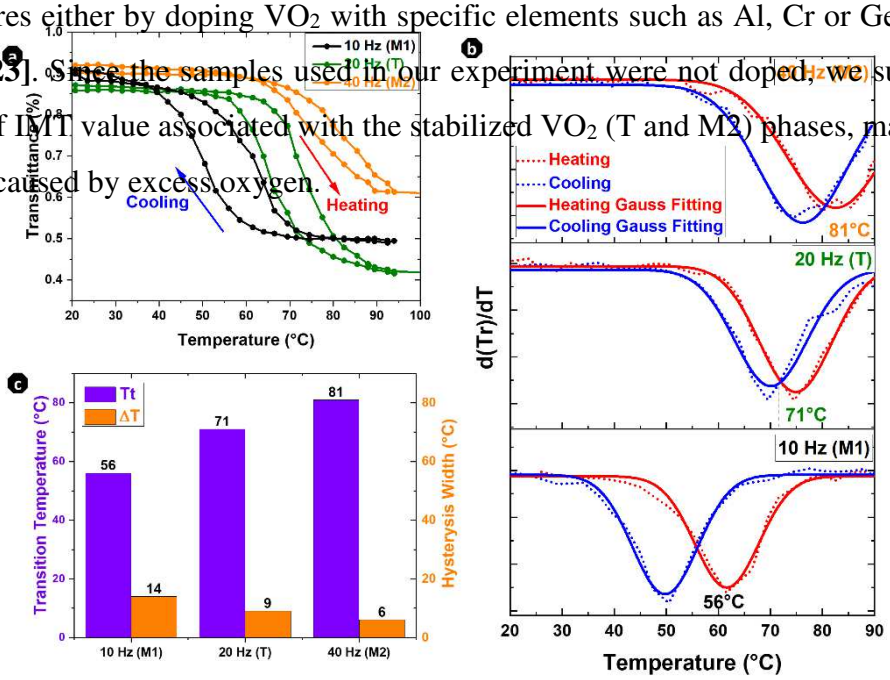

Figure 8. (a) Temperature-dependent IR transmittance, hysteresis curves at 2000 nm of the three VO_2 phases. (b) Plots of d(Tr)/d(T)&T vs Temperature with Gaussian fitting (solid lines). (c) Phase transition temperatures and hysteresis width as a function of the VO_2 phases.

What is more, the size of the VO_2 crystallite and its distribution can affect the width and shape of hysteresis. More precisely, a high-quality VO_2 crystal and narrow crystallite size distribution has been shown to result in a narrow hysteresis loop and vice versa**[45]**. Comparing the AFM and SEM morphologies, the VO_2 (M1) presents a larger hysteresis loop with bigger grain size and greater roughness than the two other VO_2 phases that have a

smaller hysteresis loop with a smoother surface and probably a smaller grain size. Our results are thus consistent with the observation made in the abovementioned studies.

Other important parameters for the thermochromic smart window are solar modulation ability (ΔT_{sol}, 380–2500 nm) and luminance transmittance (T_{lum}, 380–780 nm). These two parameters can be calculated from temperature-dependent vis-IR spectra via equation 4 and 5:

$$T_{lum,sol} = \frac{\int \varphi_{lum,sol}(\lambda)T(\lambda)d\lambda}{\int \varphi_{lum,sol}(\lambda)d\lambda} \quad (4)$$

$$\Delta T_{sol} = T_{sol,\,lt} - T_{sol,\,ht} \text{ and } T_{lum} = (T_{lum}(lt) + T_{lum}(ht))/2 \quad (5)$$

where $T(\lambda)$ denotes thin film transmittance at a given wavelength (λ), $\varphi_{lum}(\lambda)$ is the standard luminous efficiency function for the photopic vision of the human eye, $\varphi_{sol}(\lambda)$ is the solar irradiance spectrum for air mass 1.5 corresponding to the sun positioned 37° above the horizon**[46]**.

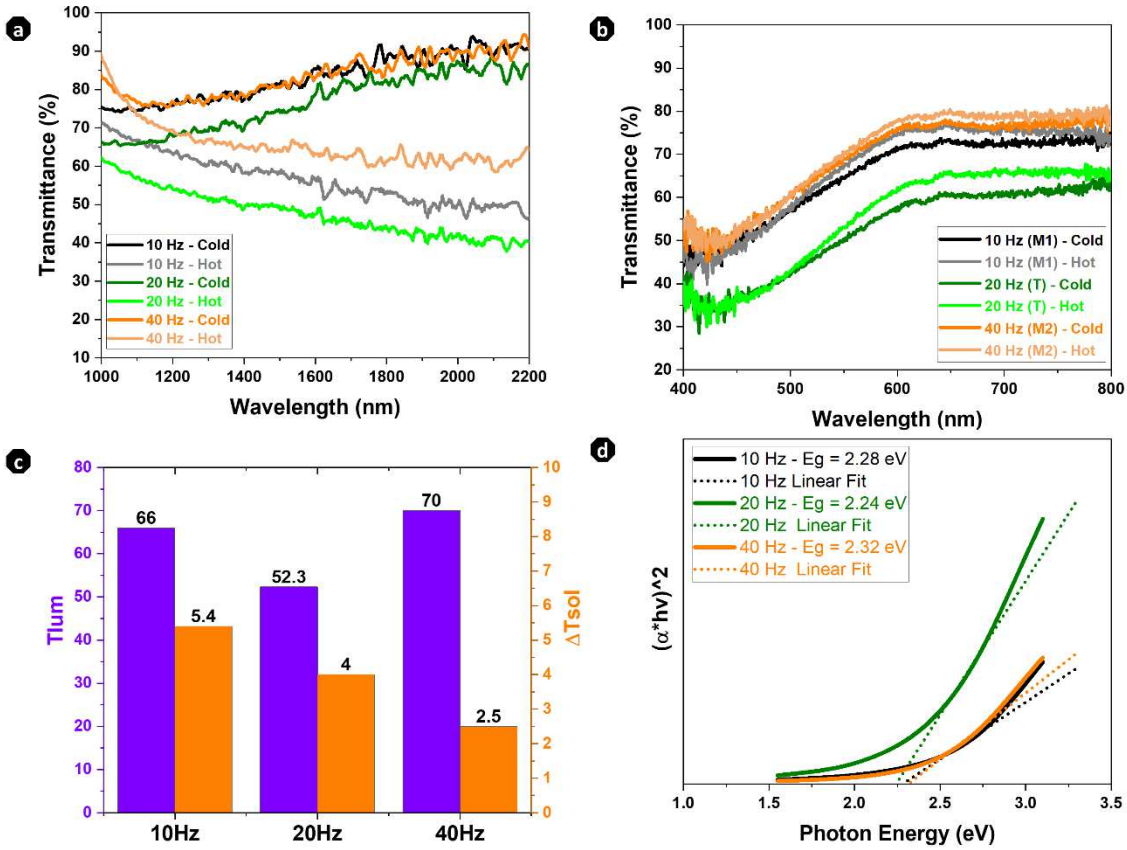

Figure 9. (a) IR spectra of VO_2 (M1, T, M2) at room temperature (cold state) and 90 °C (hot state). (b) Visible spectra of VO_2 (M1, T, M2) at room temperature (cold state) and 90 °C (hot state). (c) Luminous transmittance at low temperatures (T_{lum}) for each VO_2 thin film phase, along with the solar modulation ability (ΔT_{sol}). (d) Tauc plot of $(\alpha E)^2$ vs photon energy to obtain the direct bandgap of VO_2 for each VO_2 thin film phase.

The IR spectra of the three samples at room temperature and 90 °C are shown in Fig. 9b. At room temperature, VO_2 thin films were in their different insulating phases (M1, T, M2) and displayed good transparency in the IR range. Interestingly, at room temperature, IR transmittance for M1 and M2 was almost superposed, while the T phase showed the least IR transmittance at room temperature. At higher temperatures, the IR transmittance in all the VO_2 phases dropped significantly, thereby confirming the transition from their insulating phases to the metallic phase; their luminous transmittance (T_{lum}) and the change in solar irradiation transmittance (ΔT_{sol}) are shown in Fig. 9c. Compared to the VO_2 (M1), the luminous transmittance of the T phase decreased from 66% to 52%, while that of the M2 phase increased from 66% to 70%. Indeed, the transmittance in the visible region shown in Fig. 9b followed the same trend as the IR transmittance. The T phase film exhibits the lower transmittance, whereas M1 and M2 phases have almost similar transmittance. The decrease in the luminous transmittance in the T phase may be due to its morphology, as surface cracks were revealed by SEM. The deterioration of transmittance of thin films has been reported to be due to a severe cracking, which results in light scattering**[47]**. In addition, going from M1 to M2, ΔT_{sol} decreased from 5.4% to 2.5%. These ΔT_{sol} are consistent with recently reported values for PLD VO_2 thin films**[48]**.

Light response behavior is also linked to the intrinsic bandgap of materials, which in turn, is directly linked to transmittance according to the following relationship: $(\alpha\hbar\nu)^n = A(\hbar\nu - Eg)$, where α is absorption factor, $\hbar\nu$ is photon energy, n = 1/2, 1/3, 2, and 2/3 for the indirect allowed, indirect forbidden, direct allowed and direct forbidden optical transitions, respectively. A is constant, and E_g is the optical bandgap of the material**[49,50]**. The plot of $(\alpha\hbar\nu)^2$ vs photon energy is shown in Fig. 8c. It is worth noting that the reflection was neglected in our Tauc plot. The direct optical band gap (2.32 eV) for the VO_2 (M2) thin film is slightly larger than the two other phases with the values of 2.28 and 2.24 eV for the M1 and T phases, respectively. These values are consistent with the previous report on VO_2 **[49,50]**. Indeed, according to another previous work, the increase of the optical band gap induces a blue shift and an improved visible transmittance**[51]**. This could explain the higher visible transmittance of the VO_2 (M2) thin film phase.

4. Conclusion

To summarize, we have shown that the three polymorphs of VO_2 (M1, T, and M2) thin films can be stabilized in a single phase using pulsed laser deposition by tuning the ablation plasma

composition by varying the laser repetition rate on the V_2O_5 target. These instances of phase stabilization were evidenced by Raman measurements. Of outstanding importance are our results showing distinct transition temperatures of 56 °C, 71 °C and 81 °C linked to the M1, T and M2 phases, respectively. Our paper describes a systematic approach for structural, morphological, nanomechanical and IMT tuning of different VO_2 thin film phases. It demonstrates that the properties analyzed are highly dependent on the VO_2 phases and their surface morphology. As these phases are associated with different surface, nanomechanical and optical properties, our work may open the way for the growth of novel functional polymorphic VO_2 with tunable IMT and functionalities.

Acknowledgments

This work was supported by the LABEX MANUTECH-SISE (ANR-10-LABX-0075) of Université de Lyon, within the Plan France 2030 operated by the French National Research Agency (ANR).

References

[1] S. Lee, I.N. Ivanov, J.K. Keum, H.N. Lee, Epitaxial stabilization and phase instability of VO2 polymorphs, Sci Rep. 6 (2016) 19621. https://doi.org/10.1038/srep19621.

[2] Ch. Leroux, G. Nihoul, G. Van Tendeloo, From VO2(B) to VO2(R):Theoretical structures of VO2 polymorphs and in situ electron microscopy, Phys. Rev. B. 57 (1998) 5111–5121. https://doi.org/10.1103/PhysRevB.57.5111.

[3] E. Baudrin, G. Sudant, D. Larcher, B. Dunn, J.-M. Tarascon, Preparation of Nanotextured VO2[B] from Vanadium Oxide Aerogels, Chem. Mater. 18 (2006) 4369–4374. https://doi.org/10.1021/cm060659p.

[4] R. Shi, Y. Chen, X. Cai, Q. Lian, Z. Zhang, N. Shen, A. Amini, N. Wang, C. Cheng, Phase management in single-crystalline vanadium dioxide beams, Nat Commun. 12 (2021) 4214. https://doi.org/10.1038/s41467-021-24527-5.

[5] A.O. Suleiman, S. Mansouri, J. Margot, M. Chaker, Tuning VO2 phase stability by a combined effect of Cr doping and oxygen pressure, Applied Surface Science. 571 (2022) 151267. https://doi.org/10.1016/j.apsusc.2021.151267.

[6] T.J. Huffman, C. Hendriks, E.J. Walter, J. Yoon, H. Ju, R. Smith, G.L. Carr, H. Krakauer, M.M. Qazilbash, Insulating phases of vanadium dioxide are Mott-Hubbard insulators, Phys. Rev. B. 95 (2017) 075125. https://doi.org/10.1103/PhysRevB.95.075125.

[7] K. Liu, S. Lee, S. Yang, O. Delaire, J. Wu, Recent progresses on physics and applications of vanadium dioxide, Materials Today. 21 (2018) 875–896. https://doi.org/10.1016/j.mattod.2018.03.029.

[8] R. Shi, N. Shen, J. Wang, W. Wang, A. Amini, N. Wang, C. Cheng, Recent advances in fabrication strategies, phase transition modulation, and advanced applications of vanadium dioxide, Applied Physics Reviews. 6 (2019) 011312. https://doi.org/10.1063/1.5087864.
[9] S. Zhang, I.S. Kim, L.J. Lauhon, Stoichiometry Engineering of Monoclinic to Rutile Phase Transition in Suspended Single Crystalline Vanadium Dioxide Nanobeams, Nano Lett. 11 (2011) 1443–1447. https://doi.org/10.1021/nl103925m.
[10] Y. Wang, X. Sun, Z. Chen, Z. Cai, H. Zhou, T.-M. Lu, J. Shi, Defect-engineered epitaxial VO2±δ in strain engineering of heterogeneous soft crystals, Science Advances. 4 (2018) eaar3679. https://doi.org/10.1126/sciadv.aar3679.
[11] J.B. MacChesney, H.J. Guggenheim, Growth and electrical properties of vanadium dioxide single crystals containing selected impurity ions, Journal of Physics and Chemistry of Solids. 30 (1969) 225–234. https://doi.org/10.1016/0022-3697(69)90303-5.
[12] J.P. Pouget, H. Launois, T.M. Rice, P. Dernier, A. Gossard, G. Villeneuve, P. Hagenmuller, Dimerization of a linear Heisenberg chain in the insulating phases of V1−xCrxO2, Phys. Rev. B. 10 (1974) 1801–1815. https://doi.org/10.1103/PhysRevB.10.1801.
[13] W. Brückner, U. Gerlach, W. Moldenhauer, H.P. Brückner, N. Mattern, H. Oppermann, E. Wolf, Phase transitions and semiconductor-metal transition in V1−xGaxO2 Single Crystals, Physica Status Solidi (a). 38 (1976) 93–102. https://doi.org/10.1002/pssa.2210380110.
[14] J.M. Atkin, S. Berweger, E.K. Chavez, M.B. Raschke, J. Cao, W. Fan, J. Wu, Strain and temperature dependence of the insulating phases of VO2 near the metal-insulator transition, Phys. Rev. B. 85 (2012) 020101. https://doi.org/10.1103/PhysRevB.85.020101.
[15] B. Hu, Y. Ding, W. Chen, D. Kulkarni, Y. Shen, V.V. Tsukruk, Z.L. Wang, External-Strain Induced Insulating Phase Transition in VO2 Nanobeam and Its Application as Flexible Strain Sensor, Advanced Materials. 22 (2010) 5134–5139. https://doi.org/10.1002/adma.201002868.
[16] H. Miyazaki, I. Yasui, Effect of buffer layer on VOx film fabrication by reactive RF sputtering, Applied Surface Science. 252 (2006) 8367–8370. https://doi.org/10.1016/j.apsusc.2005.11.040.
[17] Y. Muraoka, Z. Hiroi, Metal–insulator transition of VO2 thin films grown on TiO2 (001) and (110) substrates, Appl. Phys. Lett. 80 (2002) 583–585. https://doi.org/10.1063/1.1446215.
[18] C. Marini, E. Arcangeletti, D. Di Castro, L. Baldassare, A. Perucchi, S. Lupi, L. Malavasi, L. Boeri, E. Pomjakushina, K. Conder, P. Postorino, Optical properties of V1−xCrxO2 compounds under high pressure, Phys. Rev. B. 77 (2008) 235111. https://doi.org/10.1103/PhysRevB.77.235111.
[19] R. McGee, A. Goswami, B. Khorshidi, K. McGuire, K. Schofield, T. Thundat, Effect of process parameters on phase stability and metal-insulator transition of vanadium dioxide (VO2) thin films by pulsed laser deposition, Acta Materialia. 137 (2017) 12–21. https://doi.org/10.1016/j.actamat.2017.07.025.
[20] A. Srivastava, H. Rotella, S. Saha, B. Pal, G. Kalon, S. Mathew, M. Motapothula, M. Dykas, P. Yang, E. Okunishi, D.D. Sarma, T. Venkatesan, Selective growth of single phase VO2(A, B, and M) polymorph thin films, APL Materials. 3 (2015) 026101. https://doi.org/10.1063/1.4906880.
[21] J. Jian, W. Zhang, C. Jacob, A. Chen, H. Wang, J. Huang, H. Wang, Roles of grain boundaries on the semiconductor to metal phase transition of VO2 thin films, Appl. Phys. Lett. 107 (2015) 102105. https://doi.org/10.1063/1.4930831.
[22] Y. Guo, H. Xu, C. Zou, Z. Yang, B. Tong, J. Yu, Y. Zhang, L. Zhao, Y. Wang, Evolution of structure and electrical properties with annealing time in solution-based VO2 thin films, Journal of Alloys and Compounds. 622 (2015) 913–917. https://doi.org/10.1016/j.jallcom.2014.11.027.
[23] R. Basu, M. Sardar, S. Dhara, Origin of phase transition in VO2, in: Mumbai, India, 2018: p. 030003. https://doi.org/10.1063/1.5028584.
[24] R. Basu, M. Sardar, S. Bera, P. Magudapathy, S. Dhara, The role of 1-D finite size Heisenberg chains in increasing the metal to insulator transition temperature in hole rich VO2, Nanoscale. 9 (2017) 6537–6544. https://doi.org/10.1039/C7NR00729A.
[25] P. Shvets, O. Dikaya, K. Maksimova, A. Goikhman, A review of Raman spectroscopy of vanadium oxides, Journal of Raman Spectroscopy. 50 (2019) 1226–1244. https://doi.org/10.1002/jrs.5616.
[26] P. Schilbe, Raman scattering in VO2, Physica B: Condensed Matter. 316–317 (2002) 600–602. https://doi.org/10.1016/S0921-4526(02)00584-7.

[27] X. Wu, Z. Wu, C. Ji, H. Zhang, Y. Su, Z. Huang, J. Gou, X. Wei, J. Wang, Y. Jiang, THz Transmittance and Electrical Properties Tuning across IMT in Vanadium Dioxide Films by Al Doping, ACS Appl. Mater. Interfaces. 8 (2016) 11842–11850. https://doi.org/10.1021/acsami.5b12417.
[28] C. Julien, J.P. Guesdon, A. Gorenstein, A. Khelfa, I. Ivanov, The influence of the substrate material on the growth of V2O5 flash-evaporated films, Applied Surface Science. 90 (1995) 389–391. https://doi.org/10.1016/0169-4332(95)00190-5.
[29] C. Marini, E. Arcangeletti, D. Di Castro, L. Baldassare, A. Perucchi, S. Lupi, L. Malavasi, L. Boeri, E. Pomjakushina, K. Conder, P. Postorino, Optical properties of V 1 − x Cr x O 2 compounds under high pressure, Phys. Rev. B. 77 (2008) 235111. https://doi.org/10.1103/PhysRevB.77.235111.
[30] Y. Hong-Tao, F. Ke-Cheng, W. Xue-Jin, L. Chao, H. Chen-Juan, N. Yu-Xin, Effect of nonstoichiometry on Raman scattering of VO_2 films, Chinese Phys. 13 (2004) 82–84. https://doi.org/10.1088/1009-1963/13/1/015.
[31] Z. Zhang, F. Zuo, C. Wan, A. Dutta, J. Kim, J. Rensberg, R. Nawrodt, H.H. Park, T.J. Larrabee, X. Guan, Y. Zhou, S.M. Prokes, C. Ronning, V.M. Shalaev, A. Boltasseva, M.A. Kats, S. Ramanathan, Evolution of Metallicity in Vanadium Dioxide by Creation of Oxygen Vacancies, Phys. Rev. Applied. 7 (2017) 034008. https://doi.org/10.1103/PhysRevApplied.7.034008.
[32] R. Geremia, D. Karnakis, D.P. Hand, The role of laser pulse overlap in ultrafast thin film structuring applications, Appl. Phys. A. 124 (2018) 641. https://doi.org/10.1007/s00339-018-2045-z.
[33] P.S. Shewale, Y.S. Yu, The effects of pulse repetition rate on the structural, surface morphological and UV photodetection properties of pulsed laser deposited Mg-doped ZnO nanorods, Ceramics International. 42 (2016) 7125–7134. https://doi.org/10.1016/j.ceramint.2016.01.101.
[34] A.V. Moholkar, S.S. Shinde, A.R. Babar, K.-U. Sim, Y. Kwon, K.Y. Rajpure, P.S. Patil, C.H. Bhosale, J.H. Kim, Development of CZTS thin films solar cells by pulsed laser deposition: Influence of pulse repetition rate, Solar Energy. 85 (2011) 1354–1363. https://doi.org/10.1016/j.solener.2011.03.017.
[35] V. Timoshevskii, Y. Ke, H. Guo, D. Gall, The influence of surface roughness on electrical conductance of thin Cu films: An ab initio study, Journal of Applied Physics. 103 (2008) 113705. https://doi.org/10.1063/1.2937188.
[36] D.L. Mills, A.A. Maradudin, Surface roughness and the optical properties of a semi-infinite material; the effect of a dielectric overlayer, Phys. Rev. B. 12 (1975) 2943–2958. https://doi.org/10.1103/PhysRevB.12.2943.
[37] B. Pittenger, N. Erina, C. Su, Quantitative Mechanical Property Mapping at the Nanoscale with PeakForce QNM, (n.d.) 12.
[38] A. Dey, M.K. Nayak, A.C.M. Esther, M.S. Pradeepkumar, D. Porwal, A.K. Gupta, P. Bera, H.C. Barshilia, A.K. Mukhopadhyay, A.K. Pandey, K. Khan, M. Bhattacharya, D.R. Kumar, N. Sridhara, A.K. Sharma, Nanocolumnar Crystalline Vanadium Oxide-Molybdenum Oxide Antireflective Smart Thin Films with Superior Nanomechanical Properties, Sci Rep. 6 (2016) 36811. https://doi.org/10.1038/srep36811.
[39] N. Sepúlveda, A. Rúa, R. Cabrera, F. Fernández, Young's modulus of VO2 thin films as a function of temperature including insulator-to-metal transition regime, Appl. Phys. Lett. 92 (2008) 191913. https://doi.org/10.1063/1.2926681.
[40] M. Liu, S. Xie, L. Wei, M. Galluzzi, Y. Li, Q. Wang, X. Zhou, Y. Wang, J. Li, Quantitative functional imaging of VO2 metal-insulator transition through intermediate M2 phase, Acta Materialia. 195 (2020) 720–727. https://doi.org/10.1016/j.actamat.2020.06.014.
[41] J.-W. Lee, S.-K. Tien, Y.-C. Kuo, C.-M. Chen, The mechanical properties evaluation of the CrN coatings deposited by the pulsed DC reactive magnetron sputtering, Surface and Coatings Technology. 200 (2006) 3330–3335. https://doi.org/10.1016/j.surfcoat.2005.07.047.
[42] C.-C. Chen, X. Qi, W.-C. Chang, M.-G. Tsai, I.-G. Chen, C.-Y. Lin, P.-H. Wu, K.-P. Chang, The effects of pulse repetition rate on the structural, optical, and electrical properties of CIGS films grown by pulsed laser deposition, Applied Surface Science. 351 (2015) 772–778. https://doi.org/10.1016/j.apsusc.2015.06.002.

[43] H. Futaki, M. Aoki, Effects of Various Doping Elements on the Transition Temperature of Vanadium Oxide Semiconductors, Jpn. J. Appl. Phys. 8 (1969) 1008. https://doi.org/10.1143/JJAP.8.1008.
[44] F. Béteille, J. Livage, Optical Switching in VO2 Thin Films, Journal of Sol-Gel Science and Technology. 13 (1998) 915–921. https://doi.org/10.1023/A:1008679408509.
[45] V.A. Klimov, I.O. Timofeeva, S.D. Khanin, E.B. Shadrin, A.V. Ilinskii, F. Silva-Andrade, Hysteresis loop construction for the metal-semiconductor phase transition in vanadium dioxide films, Tech. Phys. 47 (2002) 1134–1139. https://doi.org/10.1134/1.1508078.
[46] B. Zhuang, Z. Dai, S. Pang, H. Xu, L. Sun, F. Ma, 3D Ordered Macroporous VO2 Thin Films with an Efficient Thermochromic Modulation Capability for Advanced Smart Windows, Advanced Optical Materials. 7 (2019) 1900600. https://doi.org/10.1002/adom.201900600.
[47] K. Narasimha Rao, Studies on thin film materials on acrylics for optical applications, Bull Mater Sci. 26 (2003) 239–245. https://doi.org/10.1007/BF02707798.
[48] H. Zong, C. Geng, C. Zhang, H. Liu, J. Wu, Z. Yu, G. Cao, C. Kang, M. Li, Tuning the electrical and optical properties of ZrxOy/VO2 thin films by controlling the stoichiometry of ZrxOy buffer layer, Applied Surface Science. 487 (2019) 138–145. https://doi.org/10.1016/j.apsusc.2019.04.115.
[49] G. r. Khan, B. a. Bhat, Quantum size effect across semiconductor-to-metal phase transition in vanadium dioxide thin films, Micro & Nano Letters. 10 (2015) 607–612. https://doi.org/10.1049/mnl.2015.0213.
[50] J. Zhou, Y. Gao, X. Liu, Z. Chen, L. Dai, C. Cao, H. Luo, M. Kanahira, C. Sun, L. Yan, Mg-doped VO2 nanoparticles: hydrothermal synthesis, enhanced visible transmittance and decreased metal–insulator transition temperature, Phys. Chem. Chem. Phys. 15 (2013) 7505–7511. https://doi.org/10.1039/C3CP50638J.
[51] M. Zhou, J. Bao, M. Tao, R. Zhu, Y. Lin, X. Zhang, Y. Xie, Periodic porous thermochromic VO2(M) films with enhanced visible transmittance, Chem. Commun. 49 (2013) 6021–6023. https://doi.org/10.1039/C3CC42112K.

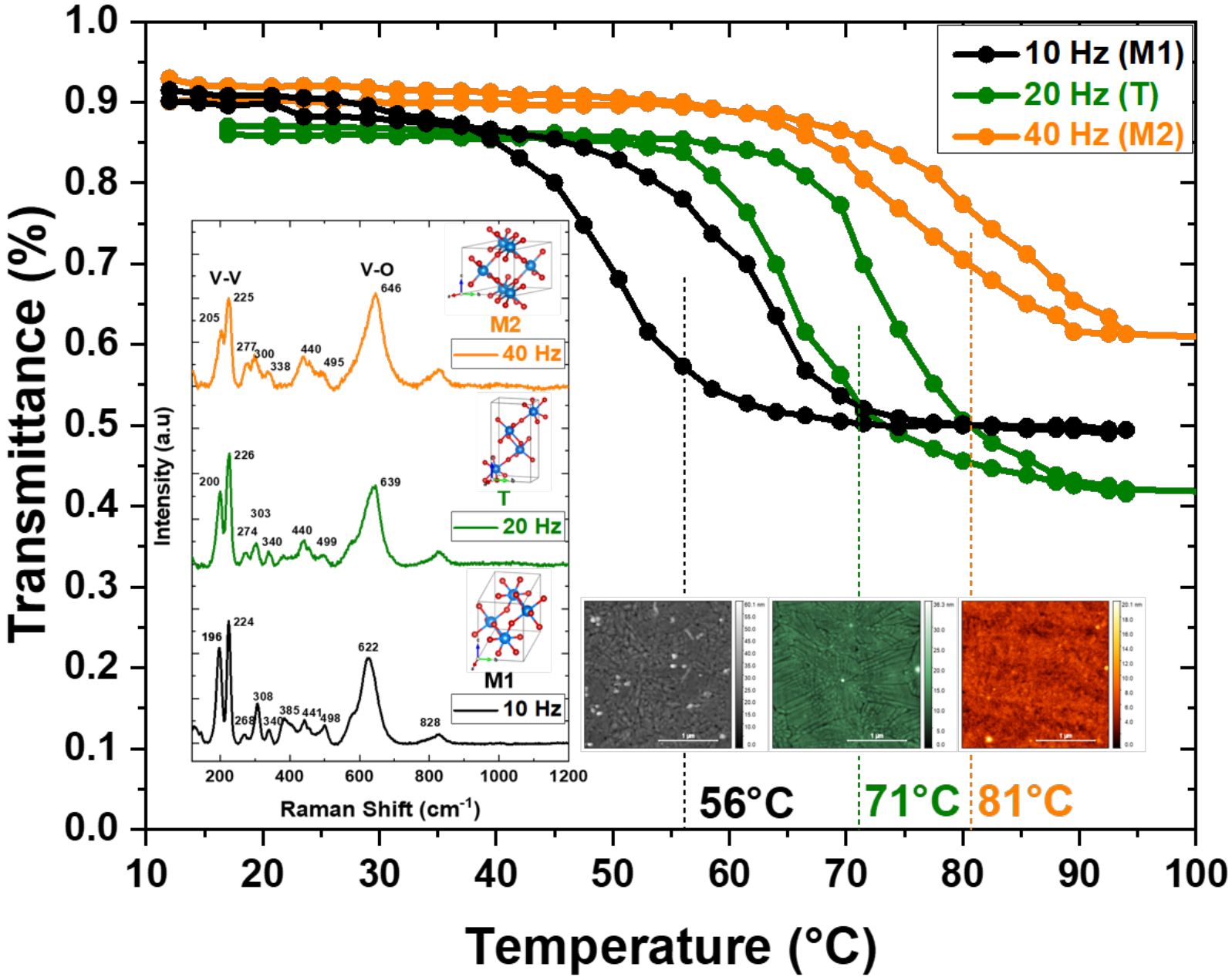
10 Hz (M1)
20 Hz (T)
40 Hz (M2)
Transmittance (%)
Temperature (°C)
1.0
0.9
0.8
0.7
0.6
0.5
0.4
0.3
0.2
0.1
0.0
10
20
30
40
50
60
70
80
90
100
Intensity (a.u)
Raman Shift (cm-1)
200
400
600
800
1000
1200
V-V
V-O
205
225
277
300
338
440
495
646
M2
40 Hz
200
226
274
303
340
440
499
639
T
20 Hz
196
224
269
308
340
385
441
498
622
828
M1
10 Hz
56°C
71°C
81°C